Dalton Transactions

PAPER

View Article Online
View Journal | View Issue

Open Access Article. Published on 19 May 2017. Downloaded on 12/5/2025 9:16:28 AM.
This article is licensed under a Creative Commons Attribution 3.0 Unported Licence.

Cite this: *Dalton Trans.*, 2017, **46**, 7693

Structure and luminescence analyses of simultaneously synthesised $(Lu_{1-x}Gd_x)_2O_2S:Tb^{3+}$ and $(Lu_{1-x}Gd_x)_2O_3:Tb^{3+}$

Natalie Pasberg,[a] Daniel den Engelsen,[b] George R. Fern,[b] Paul G. Harris,[b] Terry G. Ireland *[b] and Jack Silver[b]

Herein we describe the synthesis and luminescence of nanosized $(Lu_{1-y-x}Gd_x)_2O_2S:Tb_y$ and $(Lu_{1-y-x}Gd_x)_2O_3:Tb_y$ phosphors with y = 0.1 mol% Tb^{3+} and y = 2 mol% Tb^{3+} and x ranging between 0 and 1. The concentration of Gd^{3+} (x) was varied in steps of 0.1 (molar ratio Gd^{3+}). The samples at $0.1 < x < 0.7$ contained a mixture of $(Lu_{1-x}Gd_x)_2O_3:Tb^{3+}$ and $(Lu_{1-x}Gd_x)_2O_2S:Tb^{3+}$, while the samples at $x = 0$ contained only $Lu_2O_3:Tb^{3+}$. At $0.1 < x < 0.7$ $Lu_2O_2S:Tb^{3+}$ and $Gd_2O_2S:Tb^{3+}$ did not form a solid solution, but rather crystallised into two slightly different hexagonal structures. This behaviour has been explained in terms of segregation of Lu and Gd between the oxide and oxysulfide phases: the oxide phase is more Lu-rich whereas the second oxysulfide phase is more Gd-rich. The photoluminescence spectra of the phosphors with 0.1 mol% Tb^{3+} showed a modest colour change of the fluorescence light from cyan to green when x was increased from 0 to 1, whereas the samples of the series with 2 mol% Tb^{3+} yielded essentially green light. From this analysis it was concluded that the colour change of $(Lu_{1-x}Gd_x)_2O_2S:0.1\%Tb^{3+}$ is caused by increasing energy transfer of the $^5D_3$-level of Tb^{3+} to the charge transfer band of $(Lu_{1-x}Gd_x)_2O_2S:Tb^{3+}$ upon increasing x. Since the samples with 100% Lu consisted of pure cubic $Lu_2O_3:Tb^{3+}$, we had the opportunity to also study the symmetry-related PL of this compound. From this study we concluded that the C_2–C_{3i} doublet of the Tb^{3+} $^5D_4 \rightarrow {}^7F_5$ transition behaves in the same way as the corresponding doublet in cubic $Y_2O_3:Tb^{3+}$.

Received 9th March 2017,
Accepted 11th May 2017

DOI: 10.1039/c7dt00862g

rsc.li/dalton

Introduction

Phosphors based on the host lattices Y_2O_2S (yttrium oxysulfide) and Gd_2O_2S (gadolinium oxysulfide) have been widely used in industry, because both are ideal for rare earth activator cations. When doped with Eu^{3+}, the Y_2O_2S lattice yields a red-emitting phosphor, which has been extensively used for colour television picture tubes.[1] When Tb^{3+} is used as the dopant in Y_2O_2S and Gd_2O_2S, the emission is in the bluish-white or green range and these phosphors have been exploited for X-ray detection and some CRT-applications.[2–5] We found that $Y_2O_2S:Tb^{3+}$ has a high cathodoluminescence (CL) luminous efficacy of about 40 lm W^{-1}, which made it a candidate as green phosphor for field emission displays.[6] The X-ray application is due to the favourable properties of these Tb^{3+}-activated phosphors, which include high density, high radiation stability, high conversion efficiency from X-ray wavelengths to visible light, and midrange decay times.[7,8] $Gd_2O_2S:Tb^{3+}$ is the most frequently employed phosphor in X-ray intensifying screens;[9] its high density of 7.44 g cm^{-3} makes it an effective trap of the incident X-ray photon, allied with this are its further attributes of high intrinsic conversion efficiency (20%) and the high quantum yield of Tb^{3+} activator ions. We have described previously that the composition of the lanthanide-based oxysulfide host lattice and the concentration of the Tb^{3+} dopant cations have a significant influence on the emission colours, which can range from blue to green.[2–5] An interesting example has been studied recently in our laboratories, *viz.* $(Y_{1-x}Gd_x)_2O_2S$ doped with $0.1\%Tb^{3+}$, in which the colour could precisely be tuned by changing the ratio between Y and Gd.[10] Over the whole range of compositions between $x = 0$ and $x = 1$ $(Y_{1-x}Gd_x)_2O_2S$ formed solid solutions, satisfying Vegard's law.

The reasons for extending our investigations to the Lu-based phosphor system were firstly that Lu is at the end of the rare earth series, having the largest atomic number and smallest ion radius and secondly that Lu^{3+} has a full 4f electron shell like Y^{3+}, which has no 4f electrons, and Gd^{3+}, which has a half filled 4f shell of 7 unpaired electrons. This implies that

---

[a] *Department of Chemical Engineering, University of Applied Sciences Münster, Stegerwaldstrasse 39, D-48565 Steinfurt, Germany*
[b] *Centre for Phosphor and Display Materials, Wolfson Centre for Materials Processing, Brunel University London, Uxbridge, Middlesex, UB8 3PH, UK. E-mail: terry.ireland@brunel.ac.uk*

This journal is © The Royal Society of Chemistry 2017

Open Access Article. Published on 19 May 2017. Downloaded on 12/5/2025 9:16:28 AM. This article is licensed under a Creative Commons Attribution 3.0 Unported Licence.

these cations will not interfere with the Tb^{3+} emission properties directly, in contrast to other lanthanide (Ln^{3+}) cations. As Lu has the largest atomic number of the lanthanide elements, Lu-compounds that are isomorphic with Gd-compounds have larger densities: the density of Gd_2O_2S is 7.32 g cm^{-3} and that of Lu_2O_2S is 8.9 g cm^{-3}. The high density of Lu_2O_2S is advantageous for the applications in X-ray intensifying screens.

Lu_2O_2S doped with rare earth ions was prepared by solid state reaction and hydrothermal methods. Zhao *et al.*[11] prepared $Lu_2O_2S:Ce^{3+}$ by annealing Lu-oxalate in a reducing atmosphere with S; Wang *et al.*[12] and Zhang *et al.*[13] prepared $Lu_2O_2S:Eu^{3+}$ by annealing a hydrothermally-prepared inorganic–organic precursor in a N_2/H_2 atmosphere. The XRD-analyses of these oxysulfides did not show impurities such as Lu_2O_3. Because of these successful syntheses, we decided to prepare $(Lu_{1-x}Gd_x)_2O_2S:Tb^{3+}$ by annealing the rare earth hydroxy-carbonate precursors with S and Na_2CO_3, as we did in our studies of $(Y_{1-x}Gd_x)_2O_2S:Tb^{3+}$.[2–6,10] We expected to synthesize only $(Lu_{1-x}Gd_x)_2O_2S:Tb^{3+}$, however it soon became apparent that in this phosphor system the preparation chemistry was not simple unlike, our previous studies on the $(Y_{1-x}Gd_x)_2O_2S:Tb^{3+}$ phosphors. Initially we did not intend to prepare $(Lu_{1-x}Gd_x)_2O_3:Tb^{3+}$ phosphors; however, when we discovered that our samples contained mixtures of oxysulfide and oxide phases, we decided to analyse both phases.

Experimental

Nanometre-sized $(Lu_{x-1}Gd_x)_2O_2S:Tb^{3+}$ phosphor particles with $0 \leq x \leq 1$ in increments of 0.1 and Tb^{3+} concentrations of 0.1 and 2 mol% were synthesised using a process based on the homogenous urea precipitation method that we have previously described.[2,3,10] The following chemicals were used in this study: lutetium oxide and terbium oxide (99.99%, Neomaterials, UK) and gadolinium oxide (99.99%, Ampere Industrie, France); nitric acid (AnalaR, Fisher Scientific, UK), urea (99.9%, Fisher Scientific, UK), Sulfur (99.5%, Sigma Aldrich, UK) and sodium carbonate (98%, Alfa Aesar, UK). All chemicals mentioned here were used without further purification. We shall use the following definition of x, being the fraction of Gd ions with respect to the total number of Gd and Lu ions: $x = n_{Gd}/(n_{Lu} + n_{Gd})$ in one mole $(Lu_{x-1}Gd_x)_2O_2S:Tb^{3+}$: so, no correction for the small amount of Tb^{3+} will be made in presenting the results.

The precipitation step required the addition of 25.0 ml stock solution $[Lu(NO_3)_3 + Gd(NO_3)_3]$ for the host lattice ions and 25.0 ml $Tb(NO_3)_3$ for the 2 mol% Tb^{3+} series or 1.25 ml $Tb(NO_3)_3$ for the 0.1 mol% Tb^{3+} series respectively. The stock solutions were diluted to 500 ml with deionised water in a 1 litre beaker, heated to a temperature of 90 °C and 15 g urea was then added. When turbidity was observed based on nanometre-sized $Lu_{1-x}Gd_x(OH)CO_3:Tb^{3+}$, the solutions were aged for one hour and the resulting white precipitates were filtered (without cooling) using vacuum filtration. The powder was washed three times with deionised water (~50 ml) and placed in an oven to dry at a temperature of 100 °C for 24 h giving white powder samples with a yield of about 2 g.

For calcination these precursor powders were initially mixed with a mortar and pestle for about 5 min with Na_2CO_3 (1.5 molar ratio) and sulfur (2 molar ratio) and then carefully placed on the bottom of an alumina crucible. To protect this bottom layer from oxidation during the calcination, it was capped with a cover layer. This cover layer consisted of a mixture of Lu_2O_3, Gd_2O_3, Na_2CO_3 and sulfur powders. The total molar concentration of these rare earth oxides was equal to the molar concentration of the respective precursors. Furthermore, the ratio of Lu_2O_3 and Gd_2O_3 was adjusted to the respective Lu^{3+}/Gd^{3+} ratio of the precursors in the bottom layer. The same molar concentration of Na_2CO_3 and sulfur in the bottom layer was used in the cover layer. The addition of oxides prevented the top layer to sag and mix with the sample materials at the bottom of the crucible when the S and Na_2CO_3 melted. Each sample was calcined in a furnace and annealed for 1 h at 900 °C in air; however, calcinations at $x_{Gd} = 0$, 0.3 and 0.5 were also done at 1100 °C and 1200 °C for 2 hours to investigate the completeness of the sulfurization. After cooling the bottom layer was carefully separated from the top layer and ground with a mortar and pestle. The ground samples were washed in approx. 70 ml deionised water at 100 °C for 20 min for purification. Then the phosphors were filtered without cooling and washed 3 times with approximately 50 ml deionised water using vacuum filtration and were dried at *ca.* 100 °C. The yields of the obtained phosphors were about 1 g depending on the Lu^{3+}/Gd^{3+} ratio. The resulting oxysulfide phosphor powders had a greyish colour.

X-ray powder diffraction (XRPD) of the samples was performed using a Bruker D8 Advance X-ray powder diffractometer fitted with a copper source and LynxEye_silicon strip detector. The diffractometer was calibrated using an aluminium oxide line position standard from Bruker and the LaB_6 NIST SRM 660a line profile standard. The emission of the nickel filtered Cu source and hence the instrumental line broadening was determined by fitting the NIST standard using the TOPAS 5 software package of Bruker. The samples were scanned from 5° to 100° (2θ) for 110 minutes in steps of 0.009°. The Bruker EVA software was used to compare the diffraction peaks of the samples with reference crystallographic data. The morphology and particle size of the samples were analysed in a Zeiss Supra 35 VP (Jena, Germany) field emission scanning electron microscope (FESEM). The elemental composition of individual particles was studied by energy dispersive X-ray spectroscopy (EDS) using an EDAX (part of the Ametek Inc. groups) instrument fitted with an Octane Super lithium-drifted silicon detector.

Various $(Lu_{1-x}Gd_x)_2O_2S:Tb^{3+}$ samples were also analysed in a transmission electron microscope (TEM), model 2100F, JEOL, Japan. This microscope was operated in scanning mode (STEM) with a spot size of 0.2 nm or 1.5 nm. For the studies in the TEM copper grids coated with thin carbon films having small holes (holey carbon films) were used as substrates: these were transparent to the high-energy electrons. The TEM was

Open Access Article. Published on 19 May 2017. Downloaded on 12/5/2025 9:16:28 AM.
This article is licensed under a Creative Commons Attribution 3.0 Unported Licence.

equipped with a Vulcan™ cathodoluminescence (CL) detector of Gatan (USA) for imaging and spectroscopic purposes. This system used a Czerny-Turner spectrometer with back-illuminated CCD and a grating with 1200 lines per mm (blazed at 500 nm) for collection of CL emission spectra. Light was collected from the sample using a mirror above and below the sample, which enabled a solid angle of about 5 sr, which is almost half of a sphere.

PL spectra were measured with a Bentham Instruments dual monochromator system. Emission spectra were recorded in the range of 300 nm to 800 nm, while excitation spectra were recorded between 250 nm and 400 nm.

Results and discussion

Fig. 1 presents X-ray diffractograms of the $(Lu_{x-1}Gd_x)_2O_2S$:0.1%Tb^{3+} powder samples. The diffractograms at 5° < 2θ < 100° refer to Gd_2O_2S:0.1%Tb^{3+} (black curve) and Lu_2O_2S:0.1%Tb^{3+} (red curve) samples. The references for Gd_2O_2S (blue lines) and Lu_2O_3 (green lines) have been indicated for comparison. The reference diffractogram for Lu_2O_2S has not been inserted for reasons to be discussed below. The insert of Fig. 1 presents a detail of the X-ray diffraction (XRD) results at 26° < 2θ < 32° for $(Lu_{x-1}Gd_x)_2O_2S$:0.1%Tb^{3+} with various mole fractions of Gd^{3+} (x = 0, 0.1, 0.2, … 1). Fig. 1 indicates that for x = 0 (100% Lu) there was no Lu_2O_2S:0.1%Tb^{3+} present in the sample, but only the oxide Lu_2O_3:0.1%Tb^{3+}. The presence of both oxide and oxysulfide phases in the samples makes the insert of Fig. 1 slightly complicated at 29.2° < 2θ < 31°, because of the appearance of both the 222 diffraction peaks of cubic $(Lu_{1-x}Gd_x)_2O_3$:0.1%Tb^{3+} (from 29.3°–29.8°) and the 011 diffraction peaks of hexagonal $(Ln_{1-x}Gd_x)_2O_2S$:0.1% Tb^{3+} (from 30°–31°). For the sample without any Gd^{3+} we could not observe diffraction peaks of the oxysulfide phase. The samples with 0.1 < x < 0.7 consisted of mixtures of oxysulfide and oxide, in which the quantity of oxide decreased upon increasing x (more Gd^{3+}). The XRD-results for $(Lu_{x-1}Gd_x)_2O_2S$:2%Tb^{3+} are similar to those for the 0.1%Tb^{3+} series and will therefore not be reproduced here.

222 OX and 011 OS refer to the diffraction peaks of the oxide and oxysulfide phases respectively.

The XRD-data were analysed with Bruker's TOPAS 5 software in order to retrieve cell dimensions, bond distances and composition of the samples. This analysis indicated that the oxysulfide in the various samples consisted of two phases, both hexagonal, but possessing slightly different structures. In Fig. 2 it is apparent that the oxysulfide XRD-peaks of the $(Lu_{0.7}Gd_{0.3})_2O_2S$:2%Tb^{3+} sample were doublets. These oxysulfide peaks were deconvoluted based on pseudo-Voigtian

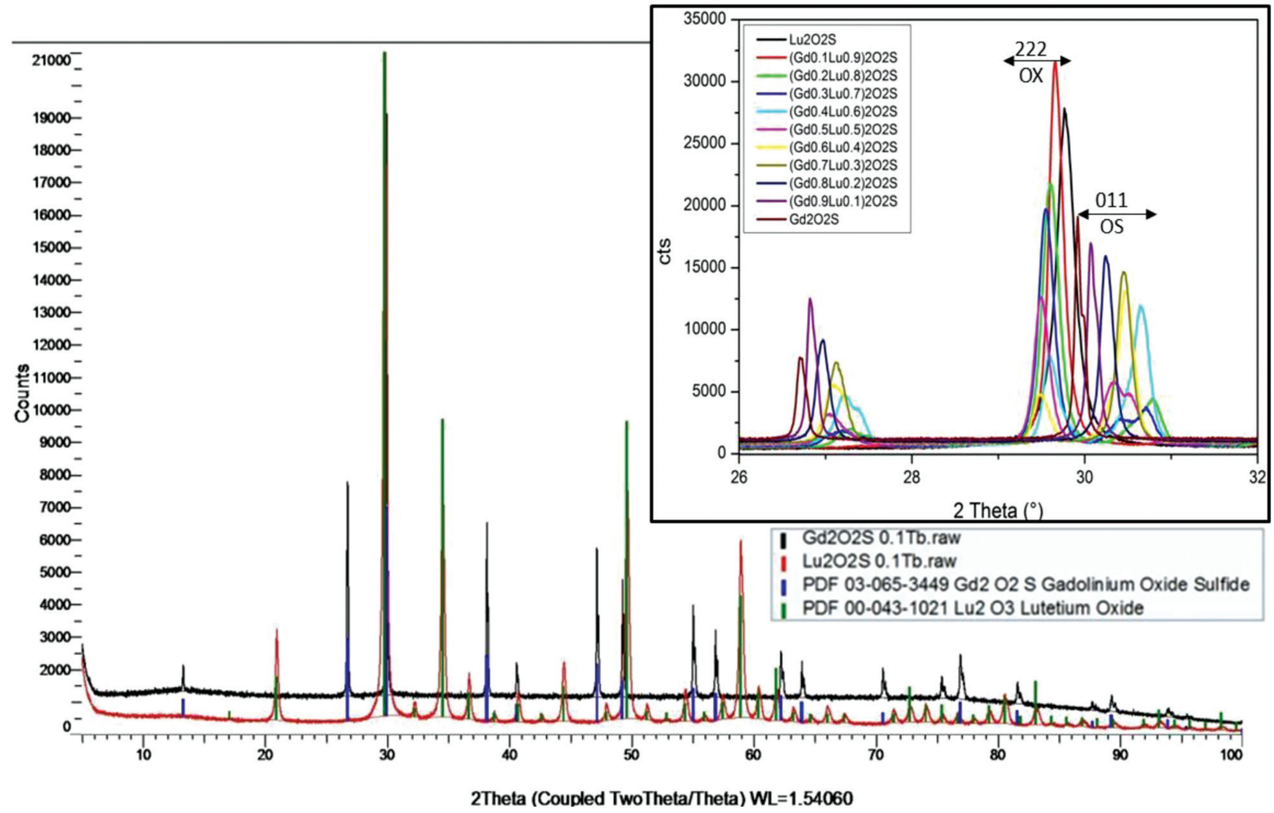

Fig. 1 XRD-data of $(Lu_{x-1}Gd_x)_2O_2S$:0.1%Tb^{3+}. The spectra at 5° < 2θ < 100° refer to Gd_2O_2S:0.1%Tb^{3+} (black curve), Lu_2O_2S:0.1%Tb^{3+} (red curve) and the references for Gd_2O_2S (blue lines) and Lu_2O_3 (green lines). The spectra of the insert at 26° < 2θ < 32° refer to $(Lu_{x-1}Gd_x)_2O_2S$:0.1%Tb^{3+} for x = 0, 0.1, 0.2, … 1.

Open Access Article. Published on 19 May 2017. Downloaded on 12/5/2025 9:16:28 AM.
This article is licensed under a Creative Commons Attribution 3.0 Unported Licence.

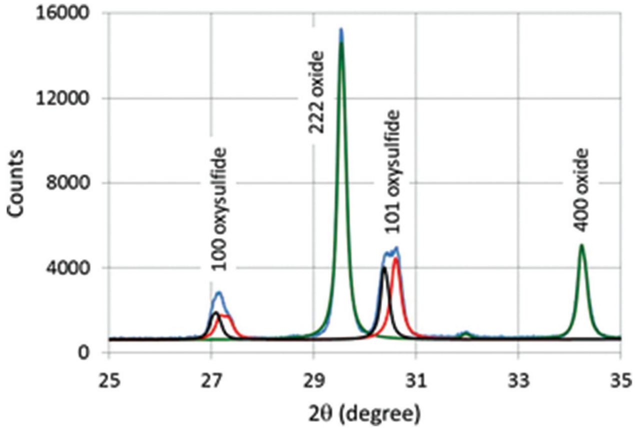

Fig. 2 Partial XRD-diagram of $(Lu_{0.7}Gd_{0.3})_2O_2S$:2%Tb^{3+}. Only the part 25° < 2q < 35° is shown for reasons of clarity. Green spectrum: oxide; blue curve: total oxysulfide; red and black spectra: oxysulfide deconvoluted.

profiles for the components and this enabled the calculation of cell parameters and concentration of the two structures of the oxysulfide, denoted by OS-1 and OS-2. The doublet structure of the oxysulfide peaks was found in samples with $0.1 < x < 0.7$. The OS-2 oxysulfide refers to the phase with the largest cell constants, yielding the lowest 2θ-value of a doublet. It should be mentioned that the shape of the oxysulfide peaks in the diffractograms excluded strain broadening; however, apparent line broadening due to a range of oxysulfide structures with slightly different cell constants cannot be ruled out. As will be shown hereafter, this does not change the analyses and conclusions.

The results of the XRD-analyses have been listed in Tables 1 and 2, of which the columns 2–9 present the same type of information. In the columns 2–4 the composition of the samples has been listed. Column 5 represents the cell constant of the cubic oxide phase; columns 6–9 list the "a" and "c" cell dimensions of the two hexagonal oxysulfide phases in the samples. Table 2 also contains data of repeat experiments and the result of an experiment, in which $(Lu_{0.4}Gd_{0.6})_2O_3$:Tb^{3+} was annealed with S at 900 °C (note 5). Finally, Table 3 contains the results of some separate preparations of $(Lu_{1-x}Gd_x)_2O_3$:2% Tb^{3+}, in which no S was added during annealing at 1020 °C for 4 hours. These materials were made in order to better understand the reactions during annealing, as will be discussed below.

The data presented in Tables 1–3 have been visualised in Fig. 3 and 4. Fig. 3 shows the composition of $(Lu_{x-1}Gd_x)_2O_2S$:Tb^{3+} for both the 0.1%Tb^{3+} and 2%Tb^{3+} series. This figure shows evidence that the sulfurization process during annealing is incomplete at $x < 0.7$: at $x = 0$ (100% Lu) the yield of oxysulfide was nil for both Tb^{3+} series. At higher annealing temperatures of 1100 °C and 1200 °C it was also impossible to make any oxysulfide at $x = 0$. At $x > 0$ the oxide content in the samples decreased; however, the monotonic decrease of the oxide content *versus* x was interrupted at $x = 0.5$ in both Fig. 3a and 3b. In Table 2 we have added some repeat trials of the annealing process with S and Na_2CO_3. At higher temperature the yield of oxysulfide was even lower at $x = 0.3$ and $x = 0.5$, while in a second synthesis at 900 °C for the $x = 0.4$ sample we could not repeat the previous result. This indicated that the synthesis of the $(Lu_{x-1}Gd_x)_2O_2S$:Tb^{3+} samples at $0 < x < 0.7$ could not be controlled satisfactorily from a yield point of view. In spite of this unsatisfactory result, it was felt that the samples were valuable for spectroscopic analyses.

Fig. 4a is Vegard's plot of the cell constant "a" of the hexagonal phases present in the $(Lu_{x-1}Gd_x)_2O_2S$:Tb^{3+} samples of both the 0.1%Tb^{3+} and 2%Tb^{3+} series; Vegard's plot of the cell constant of the cubic oxide $(Lu_{x-1}Gd_x)_2O_3$:Tb^{3+}, which is present in the samples, is shown in Fig. 4b. Since the cell constant c of the hexagonal oxysulfide yielded essentially the same information as the cell constant a, Vegard's plot of c has not been represented. For reasons of comparison the cell parameters a for $(Y_{x-1}Gd_x)_2O_2S$:0.1%Tb^{3+} have been inserted in Fig. 4a.[10] The curves for $(Lu_{x-1}Gd_x)_2O_2S$:Tb^{3+} OS-2 show substantial deviations from Vegard's law at $0.2 < x < 0.7$, whereas curve 1 for the OS-1 0.1% Tb^{3+} series is closer to Vegard's law. From Fig. 4a it can be concluded that Y_2O_2S and Gd_2O_2S

Table 1 Composition and cell dimensions of oxide and oxysulfide phases in $(Lu_{1-x}Gd_x)_2O_2S$:0.1%Tb^{3+} samples

	Composition (%)			Cell dimension (Å)				
					OS-1		OS-2	
x	Oxide	OS-1	OS-2	Oxide	*a*	*c*	*a*	*c*
0	100			10.3948(11)				
0.1	97.3(2)	2.06(17)	0.60(15)	10.4235(10)	3.7190(9)	6.504(3)	3.728(2)	6.671(8)
0.2	78.3(4)	13.5(3)	8.1(4)	10.4509(15)	3.7414(6)	6.5344(11)	3.7652(7)	6.5644(15)
0.3	76.1(3)	13.7(3)	10.2(3)	10.4641(15)	3.7512(6)	6.5461(12)	3.7881(6)	6.5922(13)
0.4	32.6(3)	51.4(4)	16.0(5)	10.4587(15)	3.7619(5)	6.5580(10)	3.7807(6)	6.5828(12)
0.5	54.5(3)	21.0(3)	24.5(3)	10.4861(14)	3.8030(5)	6.6079(9)	3.7761(5)	6.5771(10)
0.6	20.5(2)	65.8(4)	13.7(4)	10.4881(14)	3.8004(5)	6.6022(10)	3.7812(5)	6.5805(9)
0.7	1.79(16)	48.1(13)	50.1(13)	10.4951(17)	3.8006(4)	6.6053(8)	3.7928(4)	6.5963(8)
0.8		100			3.8131(4)	6.6195(6)		
0.9		100			3.8341(3)	6.6458(5)		
1		100						

This journal is © The Royal Society of Chemistry 2017

Open Access Article. Published on 19 May 2017. Downloaded on 12/5/2025 9:16:28 AM. This article is licensed under a Creative Commons Attribution 3.0 Unported Licence.

Table 2 Composition and cell dimensions of oxide and oxysulfide phases in $(Lu_{1-x}Gd_x)_2O_2S$:2%Tb^{3+} samples

	Composition (%)			Cell dimension (Å)				
					OS-1		OS-2	
x	Oxide	OS-1	OS-2	Oxide	*a*	*c*	*a*	*c*
0	100			10.3948(11)[a]				
0.1	87.7(6)	8.9(3)	3.4(3)	10.4251(10)	3.7336(4)	6.5218(8)	3.7550(6)	6.5442(15)
0.2	56.2(5)	30.5(4)	13.2(40)	10.4570(10)	3.7453(4)	6.5368(6)	3.7649(4)	6.5622(9)
0.3	58.5(3)	20.5(3)	21.0(3)	10.4712(14)	3.7653(5)	6.5629(10)	3.7935(5)	6.5951(10)
0.4	14.3(3)	69.4(5)	16.3(5)	10.4955(14)	3.7839(5)	6.5836(9)	3.8012(6)	6.6048(10)
0.5	51.8(3)	22.2(3)	26.0(3)	10.4883(13)	3.7779(5)	6.5803(10)	3.8033(5)	6.6086(9)
0.6	3.5(2)	50.0(12	46.5(13)	10.5074(16)	3.7938(4)	6.5965(7)	3.8009(4)	6.6055(7)
0.7		100			3.8160(3)	6.6235(6)		
0.8		100			3.8245(3)	6.6339(5)		
0.9		100			3.8384(2)	6.6493(4)		
1		100			3.8521(5)	6.6644(8)		
0.3[b]	71.3(2)	2.18(18)	26.57(1)	10.5154(5)	3.7563(10)	6.563(3)	3.8531(2)	6.6646(3)
0.4[c]	1.31(9)	43.5(13)	55.2(13)	10.5552(17)	3.7907(5)	6.5910(9)	3.7988(6)	6.6002(8)
0.5[d]	75.5(3)	4.4(3)	20.2(2)	10.5575(8)	3.7938(8)	6.615(3)	3.8312(3)	6.6421(6)
0.6[e]	2.54 (11)	40.1(15)	57.3(15)	10.5680(18)	3.7915(6)	6.5903(12)	3.7986(6)	6.6037(11)

[a] Value taken from Table 1. [b] Repeat, annealing at 1200 °C. [c] Repeat, annealing at 900 °C. [d] Repeat, annealing at 1200 °C. [e] Annealing of $(Lu_{0.4}Gd_{0.6})_2O_3$:Tb^{3+} at 900 °C with S.

Table 3 Composition and cell constants of cubic $(Lu_{1-x}Gd_x)_2O_3$:2% Tb^{3+}

	Composition (%)		Cell constant (Å)	
x	ox-1	ox-2	ox-1	ox-2
0.3	40.6(10)	59.4(10)	10.494(20)	10.536(2)
0.5	59.4(8)	40.6(8)	10.571(4)	10.631(4)
0.6	55.9(7)	44.1(7)	10.608(3)	10.672(3)

(curve 5) form a solid solution, whereas Lu_2O_2S and Gd_2O_2S do not. It should be mentioned that this conclusion refers to the solid state reaction described in this article. It may well be that solid solutions can be obtained by other synthesis methods. The slope of curve 5 in Fig. 4a is less steep than that for the curves 1 and 3. This could be anticipated from the size of the ionic radii of the Ln^{3+} cations (6-coordinated), which are 0.86 Å, 0.90 Å, 0.92 Å and 0.94 Å for Lu^{3+}, Y^{3+}, Tb^{3+} and Gd^{3+} respectively.[14] In Fig. 4b it is apparent that the cell constant of the cubic oxide in the samples annealed with S deviates considerably from Vegard's law: the cell constant at $x > 0.1$ is much smaller than it should be according to Vegard's law. In Fig. 4b we have also plotted the cell constants of three samples that were annealed without S; these samples yielded pure oxides and the cell constants of these samples have been inserted in Fig. 4b. We found that the peaks of the cubic oxide $(Lu_{x-1}Gd_x)_2O_3$:2%Tb^{3+} in the diffractograms were also broadened due to the presence of oxide phases with slightly different cell constants, although less pronounced as in the case of the oxysulfide peaks as shown in Fig. 2. The TOPAS 5 refinements of the XRD-data were performed allowing for two

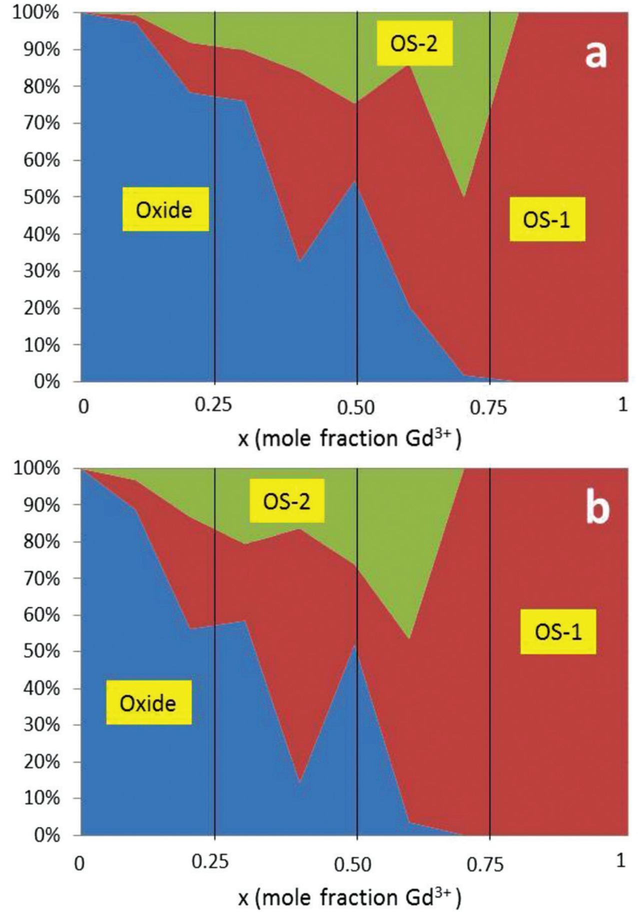

Fig. 3 Composition of $(Lu_{x-1}Gd_x)_2O_2S$:Tb^{3+}. (a) 0.1% Tb series, (b) 2%Tb series. All samples were annealed at 900 °C with sulfur, as described in the Experimental section.

Open Access Article. Published on 19 May 2017. Downloaded on 12/5/2025 9:16:28 AM.
This article is licensed under a Creative Commons Attribution 3.0 Unported Licence.

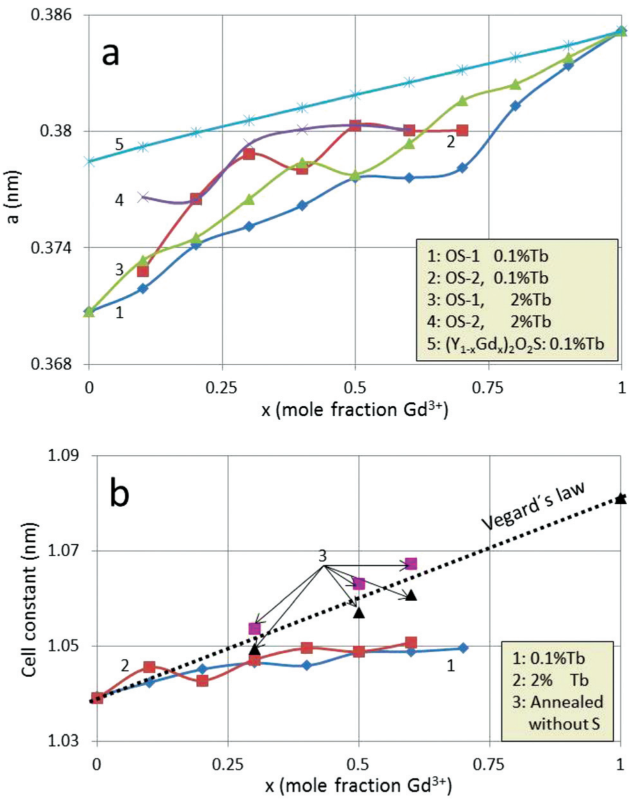

Fig. 4 Vegard's plots of cell dimensions. (a): $(Lu_{x-1}Gd_x)_2O_2S$:Tb^{3+} (curves 1–4). Curve 5 refers to $(Y_{x-1}Gd_x)_2O_2S$:0.1%Tb^{3+} (from ref. 10; it has been inserted for reasons of comparison). (b): Cell constant of oxide phase. Vegard's law is represented by the dashed line. Points 3 refer to separately annealing of the hydroxy carbonate precursor at 1020 °C without S, yielding oxide phases only.

oxide structures. Strain broadening cannot be completely ruled out for the $x = 0.3$ and $x = 0.5$ samples. We are presently investigating this behaviour in more detail and shall publish the results separately. The average of the cell constants of the two oxide structures ox-1 and ox-2, evaluated from the data in Table 3, follow Vegard's law for the system Lu_2O_3–Gd_2O_3, as can be concluded from Fig. 4b.

A hypothesis that explains the small cell constant of the oxide in the mixed samples is segregation of Lu and Gd: the oxide phase is enriched with Lu while the oxysulfide, notably the OS-2 phase, is enriched with Gd. This hypothesis is confirmed by energy dispersive X-ray (EDS) spectroscopy, to be discussed in the next section. In the discussion section we shall present an in-depth consideration on the complementary behaviour of the curves 2 and 4 for the oxysulfides in Fig. 4a in the first case and the oxide curves 1 and 2 in Fig. 4b in the second case.

In Fig. 5 FESEM images of the $(Lu_{1-x}Gd_x)_2O_2S$:0.1%Tb^{3+} samples are presented. The pure lutetium sample shown in Fig. 5a was composed of small spherical particles of about 100 nm in diameter. When the gadolinium concentration increased, the quantity of polyhedral particles became larger (Fig. 5b) and maximised at 50% gadolinium (Fig. 5c). Some cuboid particles were also present; these particles had smooth featureless faces (see Fig. 5c and d). The morphology changes presented in Fig. 5 upon increasing x illustrate the behaviour represented in Fig. 3 and 4. Small spherical oxide particles prevail at small x (Lu-rich samples), when x increases the quantity of large hexagonal particles increases, while at $x = 0.5$ large cuboid particles are abundant. It is obvious to assign these latter particles to the oxide phase; however, this assign-

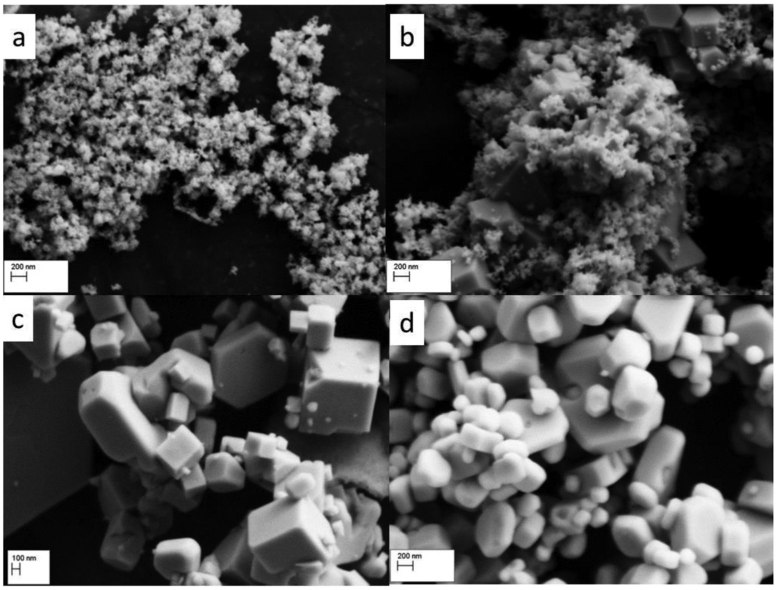

Fig. 5 FESEM images of $(Lu_{1-x}Gd_x)_2O_2S$:0.1%Tb^{3+}; (a) Lu_2O_2S (mag. 60k); (b) $(Gd_{0.1}Lu_{0.9})_2O_2S$ (mag. 60k); (c) $(Gd_{0.5}Lu_{0.5})_2O_2S$ (mag. 60k); (d) Gd_2O_2S (mag. 60k).

This journal is © The Royal Society of Chemistry 2017

Open Access Article. Published on 19 May 2017. Downloaded on 12/5/2025 9:16:28 AM.
This article is licensed under a Creative Commons Attribution 3.0 Unported Licence.

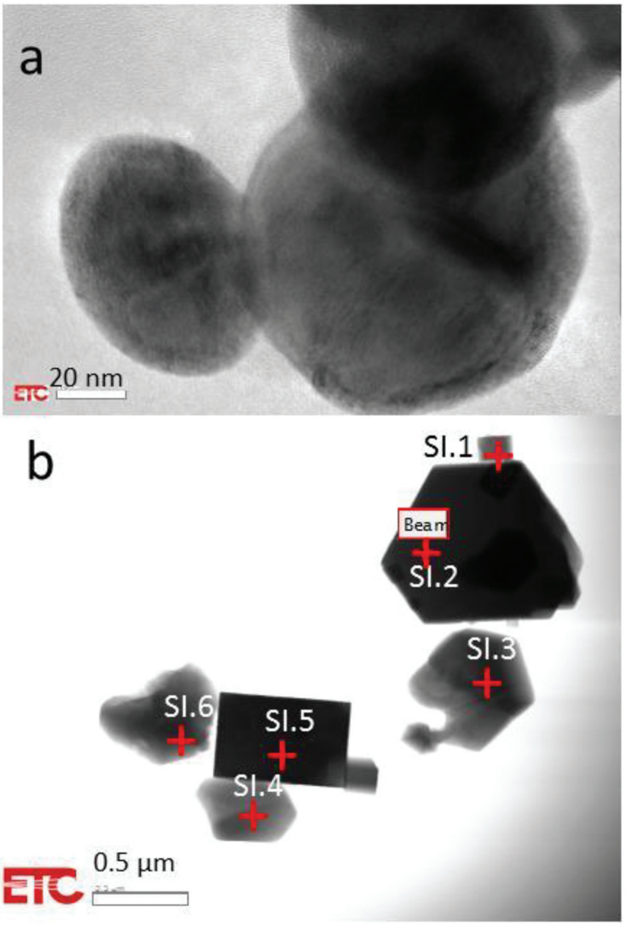

Fig. 6 (a) TEM image of $(Lu_{0.2}Gd_{0.8})_2O_2S$:0.1%Tb^{3+} (200 keV), (b) STEM bright field image of $(Lu_{0.5}Gd_{0.5})_2O_2S$:2%Tb^{3+}. SI.1, SI.2, *etc.* indicate the positions where CL-spectra have been recorded, as represented in Fig. 8b.[16]

ment has still to be verified. Moreover, it is not clear why these particles are so large. The images of $(Lu_{1-x}Gd_x)_2O_2S$:2%Tb^{3+} are similar to those of $(Lu_{1-x}Gd_x)_2O_2S$:0.1%Tb^{3+}, except that the spherical particles are slightly smaller. This is due to the larger amount of terbium ions present, the latter are known to yield smaller hydroxy carbonate precursor particles in the urea homogeneous precipitation method at terbium molar fractions >1 mol%.[15]

Fig. 6a is a highly magnified TEM image of $(Lu_{0.2}Gd_{0.8})_2O_2S$:0.1%Tb^{3+} at 200 keV, while Fig. 6b is a STEM bright field image of $(Lu_{0.5}Gd_{0.5})_2O_2S$:2%Tb^{3+}. The electron beam was positioned at various points on the crystals for recording CL-spectra; the positions are indicated by SI.1, SI.2, *etc.* in the figure. It can be seen in Fig. 6b that crystal SI.5 has a rectangular shape, whereas the other crystals have angles of 120°, which likely indicates the hexagonal structure of oxysulfide.

Fig. 6 indicates that there is a substantial range of diameters in the particles samples. This can also be observed in Fig. 5c and d. Fig. 8b presents the CL-spectra that were recorded with the Gatan spectrometer in the TEM at the various spots indicated in Fig. 6b. These spectra, which will be discussed in more detail hereafter, also confirm that the crystal SI.5 is the cubic oxide phase, whereas the other crystals are predominantly oxysulfide.

The two crystal types that can be observed in Fig. 6 were also investigated by EDS; the results of this investigation have been published recently.[16] The hexagonal crystals contain much more sulfur than the cubic crystals; this is evidence that the hexagonal crystals are oxysulfide. The sulfur signal in the EDS spectra from the cuboid crystals is much smaller and thus these crystals can be assigned to the oxide phase of the $(Lu_{0.5}Gd_{0.5})_2O_2S$:2%Tb^{3+} sample The sulfur signal did however not completely disappear when the e-beam bombarded the cubic crystals: it is assumed that the surface of these oxide crystals is contaminated with sulfur.[16]

Fig. 7 presents a selection of the excitation and emission spectra of $(Lu_{1-x}Gd_x)_2O_2S$:0.1%Tb^{3+} and $(Lu_{1-x}Gd_x)_2O_2S$:2%Tb^{3+} samples. The excitation spectra were monitored at 544 nm and the emission spectra were excited at 291 nm. The excitation spectra of the 0.1%Tb^{3+} series (Fig. 7a) manifest sharp peaks, which are attributed to Gd^{3+} transitions. These peaks are located at 275 nm, 278 nm, 280 nm (w), 291 nm (w), 308 nm and 314 nm. The first four peaks are attributed to the $^8S \rightarrow {}^6I$ transition manifold of Gd^{3+} and the last two to the $^8S_0 \rightarrow {}^6P_J$ transition manifold.[17,18] These peaks grow in intensity when x increases from 0.3 to 1. The Gd^{3+} peaks at 308 nm and 314 nm in our work on $(Y_{1-x}Gd_x)_2O_2S$:0.1%Tb^{3+} (ref. 10) were combined into one band because of the lower resolution of the spectrometer used in that study. Fig. 7c for the 2%Tb^{3+} series shows weak peaks at 379 nm, 374 nm, 368 nm, 361 nm, 355 nm, 352 nm, 244 nm and 341 nm. These peaks are attributed to Tb^{3+} transitions: the peaks between 374 nm and 341 nm from the ground state ($^7F_6$) to the ^5G_J state,[17] and the peak at 379 nm is attributed to the $^7F_6 \rightarrow {}^5D_3$ absorption.

In the excitation spectra presented in Fig. 7a and c an order-of-magnitude difference between the maximum intensities of Lu_2O_3:Tb^{3+} (x = 0) and Gd_2O_2S:Tb^{3+} (x = 1) can be observed. The monitoring wavelength of 544 nm for these spectra coincides with the C_{3i} peak of the $^5D_4 \rightarrow {}^7F_5$ transition of Lu_2O_3:Tb^{3+} and the 544 peak of Gd_2O_2S:Tb^{3+}, which means that both excitation spectra are well-optimised. The excitation spectra of the 0.1%Tb^{3+} series in Fig. 7a manifest a maximum of the charge transfer (CT) band at about 270 nm, whereas the spectra of the 2%Tb^{3+} series have their maximum at about 291 nm. This behaviour was also found in the excitation spectra of $(Y_{1-x}Gd_x)_2O_2S$:Tb^{3+}, in which the 0.1%Tb^{3+} series had its maximums at about 266 nm and the 2%Tb^{3+} series at about 290 nm.[10] The excitation spectra of $(Lu_{1-x}Gd_x)_2O_2S$:0.1%Tb^{3+} with 0 and 0.1 mole fraction of Gd^{3+} deviate clearly from those with higher Gd^{3+} content. These differences refer mainly to the intensity and the wavelength of the maximum. For the 2%Tb^{3+} series it is the 100% lutetium sample that shows the clearly-deviating excitation spectrum. The excitation spectra of the 100% lutetium samples are attributed to Lu_2O_3:Tb^{3+} and they are similar to the spectra of Y_2O_3:Tb^{3+},[19] these will be discussed in the next section. Lu_2O_3:Tb^{3+} has a cubic crystal struc-

Open Access Article. Published on 19 May 2017. Downloaded on 12/5/2025 9:16:28 AM.
This article is licensed under a Creative Commons Attribution 3.0 Unported Licence.

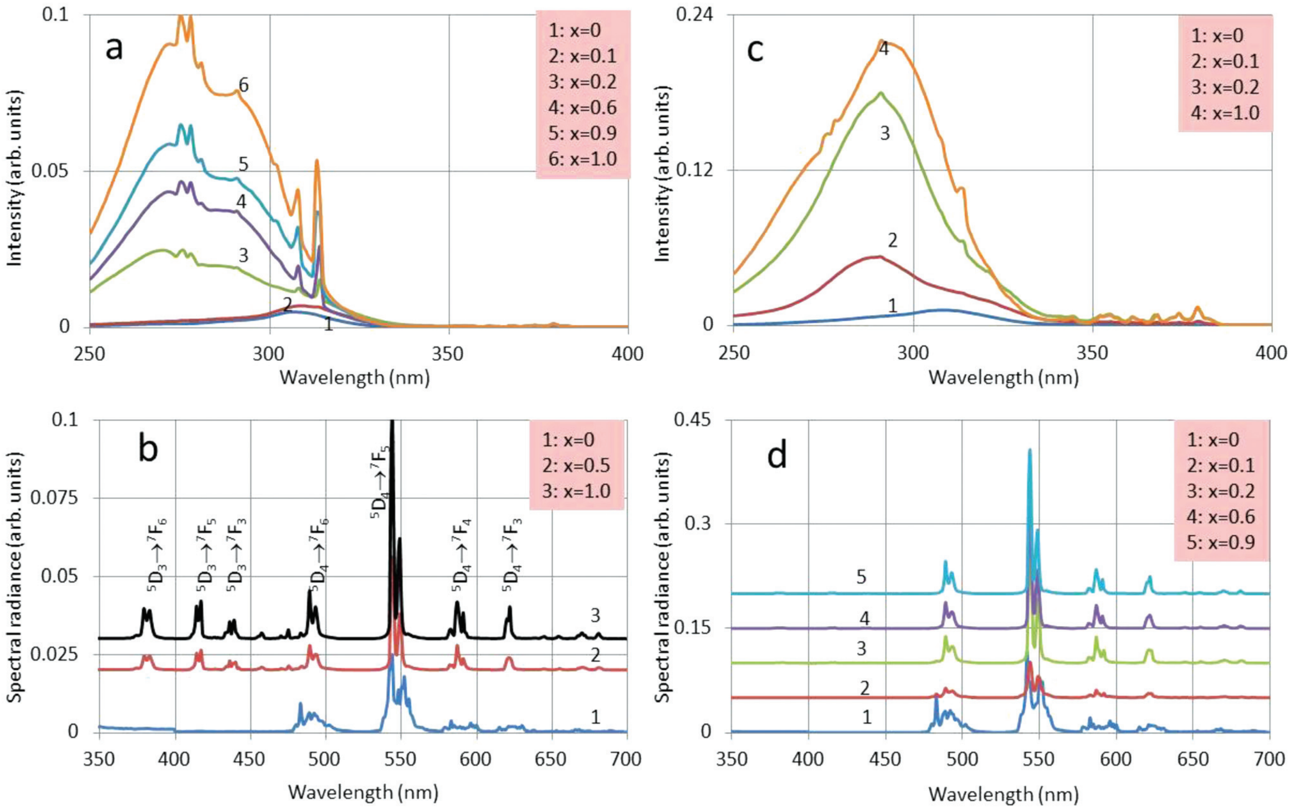

Fig. 7 Photoluminescence of $(Lu_{1-x}Gd_x)_2O_2S{:}Tb^{3+}$. (a) Excitation spectra of $(Lu_{1-x}Gd_x)_2O_2S{:}0.1\%Tb^{3+}$; (b) emission spectra of $(Lu_{1-x}Gd_x)_2O_2S{:}0.1\%Tb^{3+}$, the spectrum for $x = 0$ has been multiplied by 10; (c) excitation spectra of $(Lu_{1-x}Gd_x)_2O_2S{:}2\%Tb^{3+}$; (d) emission spectra of $(Lu_{1-x}Gd_x)_2O_2S{:}2\%Tb^{3+}$, the spectrum for $x = 0$ has been multiplied by 10. Excitation spectra monitored at 544 nm, emission spectra excited at 291 nm. Not all spectra are presented for reasons of clarity.

ture and the excitation spectrum of the Tb^{3+} cations in this structure is very different from that in the Lu_2O_2S lattice.[20,21]

In comparing the emission spectra in Fig. 7b and d it should be kept in mind that the spectra for the pure Lu-samples ($x = 0$) were about 20–30 times weaker than the oxysulfide spectra at $x > 0.4$. To facilitate comparison the spectra at $x = 0$ have been multiplied by a factor of 10. A more detailed analysis of the PL spectra of $Lu_2O_3{:}Tb^{3+}$ will be described hereafter when discussing Fig. 12.

Fig. 8 presents the PL- and CL-spectra of $(Lu_{1-x}Gd_x)_2O_2S{:}2\%Tb^{3+}$ between 470 nm and 570 nm. The PL spectra for $x = 0$ and 0.6 in Fig. 8a were excited with 291 nm UV light, while the CL-spectra in Fig. 8b were recorded with the Gatan spectrometer in the TEM at 200 keV at the various spots indicated in Fig. 6b. The spectra in Fig. 8 have been normalized using the maximum peak of the Tb^{3+} $^5D_4 \rightarrow {}^7F_5$ manifold at 544 nm for the $x = 0.6$ spectrum and at 542 nm for the $x = 0$ spectrum in Fig. 8a. This facilitates the differences between the spectra of the oxide for 100% Lu ($x = 0$) and the oxysulfide to be appreciated. It should be realized that the PL-efficiency of the oxysulfide is about 20 times larger than that of the oxide, as shown in Fig. 7d. From the CL-spectra presented in Fig. 8b it can be concluded that the spectrum from SI.5 has a clear oxide character, as it has an emission peak at 483 nm and the emission band at 545 nm has been broadened. These are the distinguishing features of the pure oxide spectrum at $x = 0$ in Fig. 8a and 12. Because of the large difference in efficiency, we also conclude from these CL-spectra that crystal SI.5 refers to the oxide phase. The oxysulfide characteristics of the SI.5-spectrum in Fig. 8b are largely caused by X-ray excitation of the neighbouring oxysulfide crystals when the e-beam is generating these rays at SI.5.

In Fig. 9 the CL spectrum of $(Lu_{0.5}Gd_{0.5})_2O_2S{:}2\%Tb^{3+}$ is presented. Although this sample also contained oxide phase (see Fig. 3), the oxysulfide spectrum in Fig. 9 is largely dominant: the 483 nm oxide line is hardly visible and the broadening of the $^5D_4 \rightarrow {}^7F_5$ manifold does not affect the doublet structure of the main line at 543 nm. Hence, it can be concluded that the spectrum shown in Fig. 9 can be attributed to $(Lu_{0.5}Gd_{0.5})_2O_2S{:}2\%Tb^{3+}$.

Fig. 10a and b show deconvolutions of the excitation spectra of $(Lu_{0.8}Gd_{0.2})_2O_2S{:}0.1\%Tb^{3+}$ with four Gaussian profiles, indicated by p1, p2, p3 and p4. It can be seen that the excitation bands $(Lu_{1-x}Gd_x)_2O_2S{:}Tb^{3+}$, consisting of the profiles p1, p2, p3 and p4, exhibit a red shift upon increasing the Gd^{3+} concentration. The red shift of the main components of the CT-band, p2 and p3, can be appreciated from the plots of wavelength against mole fraction of Gd shown in Fig. 11a and b. The horizontal axes in Fig. 11 refer to the mole fraction of Gd as weighed. When there is segregation between Lu and Gd,

Open Access Article. Published on 19 May 2017. Downloaded on 12/5/2025 9:16:28 AM.
This article is licensed under a Creative Commons Attribution 3.0 Unported Licence.

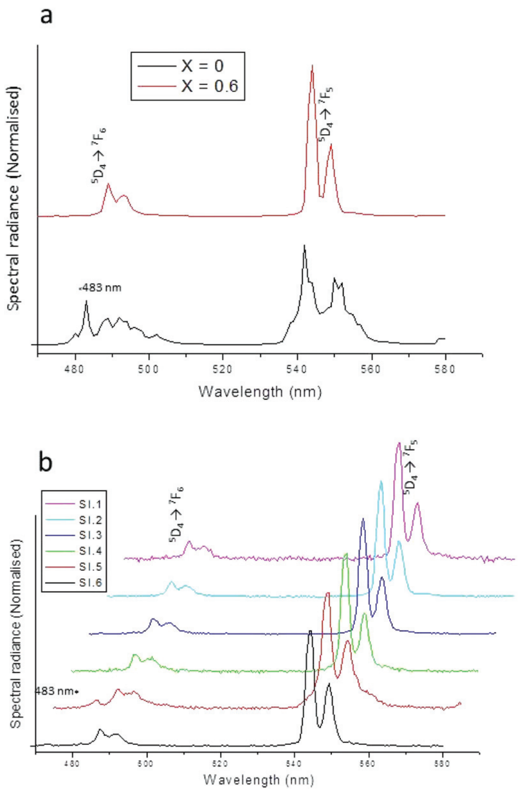

Fig. 8 (a) PL spectra of $(Lu_{1-x}Gd_x)_2O_2S$:2%Tb^{3+} between 470 nm and 570 nm with x = 0 and x = 0.6. (b) CL spectra of $(Lu_{0.5}Gd_{0.5})_2O_2S$:2%Tb^{3+} crystals shown in Fig. 6b recorded with the Gatan spectrometer of the TEM at 200 keV.[16]

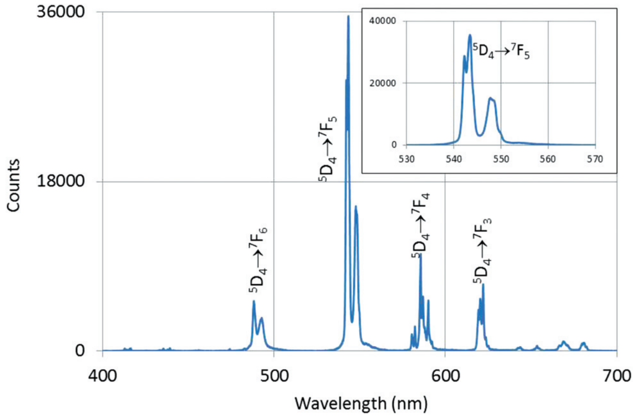

Fig. 9 High resolution CL spectrum of $(Lu_{0.5}Gd_{0.5})_2O_2S$:2%Tb^{3+} recorded at 200 keV and room temperature in the TEM. The insert shows the structure of the Tb^{3+} $^5D_4\rightarrow{}^7F_5$ manifold in more detail.

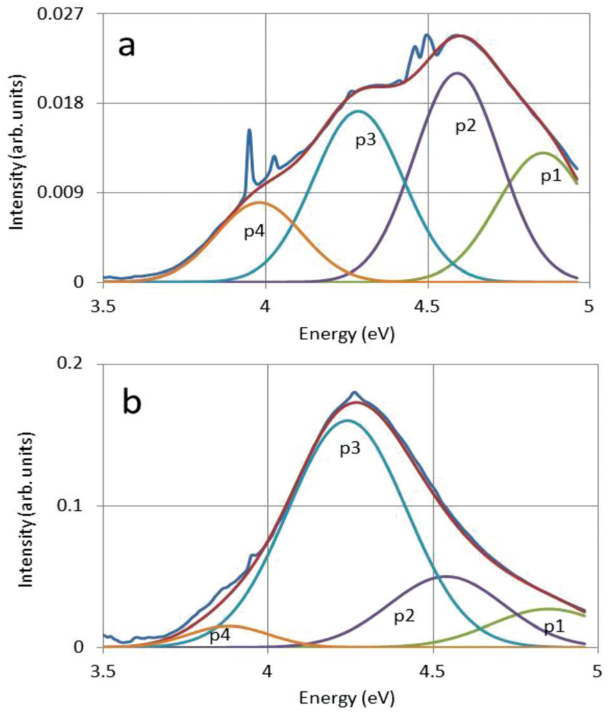

Fig. 10 Deconvolution of CT-band of $(Lu_{0.8}Gd_{0.2})_2O_2S:Tb^{3+}$ with four Gaussian profiles. (a) 0.1% Tb^{3+}; (b) 2% Tb^{3+}.

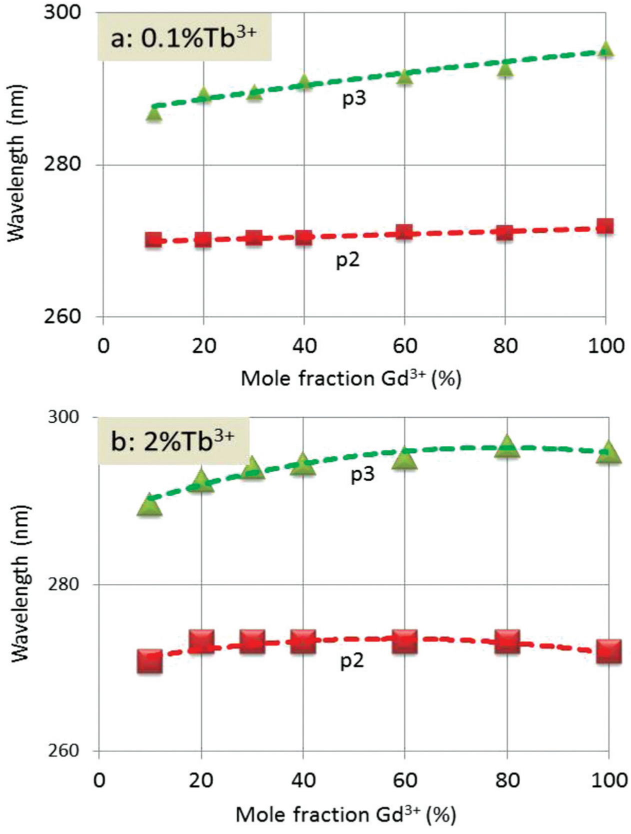

Fig. 11 Maximum of CT-band of $(Lu_{1-x}Gd_x)_2O_2S:Tb^{3+}$ *versus* x (in %). (a) 0.1% Tb^{3+} series; (b) 2% Tb^{3+} series.

as can be concluded from Fig. 4, the actual values of Gd should be corrected in Fig. 11. However, this correction has only a limited effect on the curves and it will not change the conclusions based on Fig. 11.

By analogy of the results of our study on $(Y_{1-x}Gd_x)_2O_2S:Tb^{3+}$,[10] p2 can be attributed to the charge transfer band of the oxysulfide host lattice, whereas p3 is assigned to the $4f^8\rightarrow$

Open Access Article. Published on 19 May 2017. Downloaded on 12/5/2025 9:16:28 AM.
This article is licensed under a Creative Commons Attribution 3.0 Unported Licence.

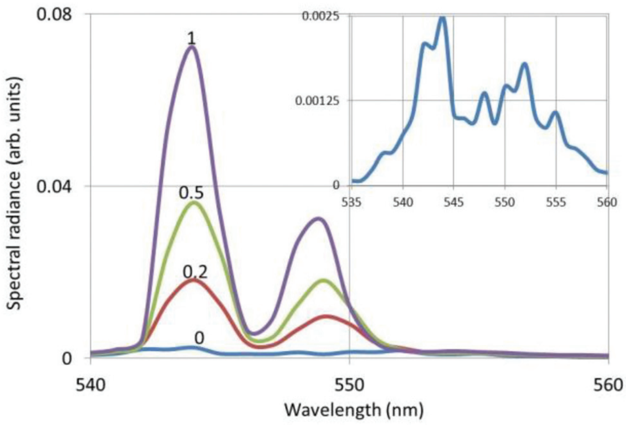

Fig. 12 $^5D_4 \rightarrow {}^7F_5$ transition of $(Lu_{1-x}Gd_x)_2O_2S$:0.1%Tb^{3+}, excited at 291 nm. The composition parameter x_{Gd} is labelling the various spectra. The insert is the spectrum for x_{Gd} = 0 (100% Lu) at 32 times larger scale.

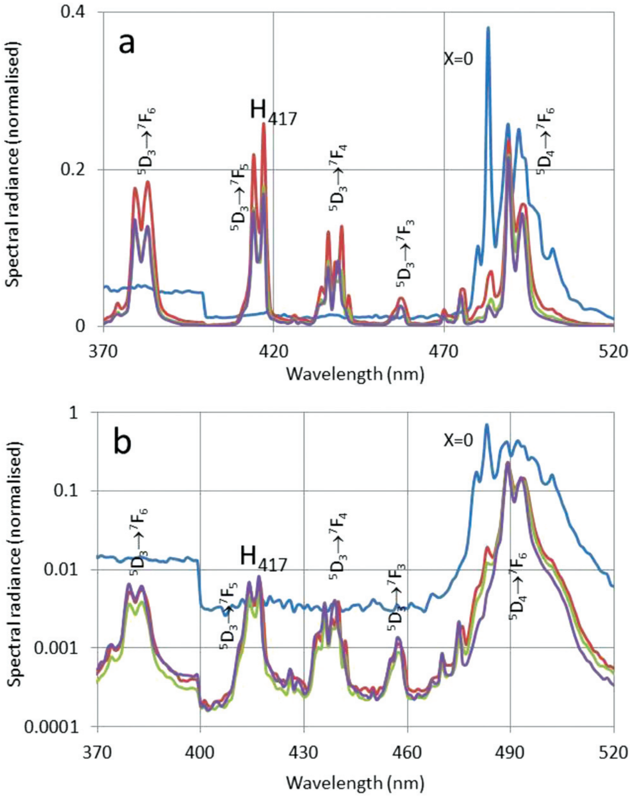

Fig. 13 $^5D_3 \rightarrow {}^7F_J$ transitions and $^5D_4 \rightarrow {}^7F_6$ transition of $(Lu_{1-x}Gd_x)_2O_2S:Tb^{3+}$ for x = 0, 0.2, 0.5 and 1. The excitation wavelength was 291 nm. (a) 0.1%Tb^{3+}; (b) 2%Tb^{3+}. Spectra have been normalised to the 544 nm peak of the $^5D_4 \rightarrow {}^7F_5$ transition, which is not represented here. The kink in the spectra at 400 nm is caused by a filter change in the Bentham monochromator.

$4f^75d$ Tb^{3+} transitions.[16,17] The red shift of p2, the CT-band, of $(Lu_{1-x}Gd_x)_2O_2S:Tb^{3+}$ in going from 10% Gd^{3+} to 100% Gd^{3+} is 1.5 nm (average of the 0.1% and 2% Tb^{3+} series), which is much less than in $(Y_{1-x}Gd_x)_2O_2S:Tb^{3+}$, where it is 5.5 nm.[10] This result will be used in Fig. 15 to explain the colour change of the PL upon changing the composition of $(Lu_{1-x}Gd_x)_2O_2S:Tb^{3+}$. The $4f^8 \rightarrow 4f^75d$ band at 291 nm shows a much larger red shift, *viz.* 7.3 nm (average). This difference in red shift between p2 and p3 confirms the different characteristics of these bands.

In Fig. 12 the $^5D_4 \rightarrow {}^7F_5$ transition of $(Lu_{1-x}Gd_x)_2O_2S$:0.1% Tb^{3+} is presented. For reasons of clarity only a limited number of spectra have been included in the figure.

The most eye-catching feature of Fig. 12 is the large difference between the spectra at $x \geq 0.2$ and the spectrum for $x = 0$ (100% Lu). This can be ascribed to the fact that the 100% Lu sample refers only to the Lu_2O_3 lattice, whereas the others are mixtures of the oxide and oxysulfide, as indicated in Tables 1 and 2 and Fig. 3a. Since the maximum spectral radiance of $Lu_2O_3:Tb^{3+}$ is about 30 times smaller than that of $Gd_2O_2S:Tb^{3+}$ (x = 1), the spectrum of the oxysulfide is already dominant at x = 0.2. The much stronger fluorescence of $Gd_2O_2S:Tb^{3+}$ as compared to that of $Lu_2O_3:Tb^{3+}$ was also found by Lempicki *et al.*[22] by X-ray excitation. They found a factor of about 7, which is smaller than the result represented in Fig. 12. It should however be kept in mind that the PL of $Lu_2O_3:Tb^{3+}$ in Fig. 12 has not been maximised by tuning the excitation wavelength to the optimum value. The second large difference between the $^5D_4 \rightarrow {}^7F_5$ transition manifolds of $Lu_2O_3:Tb^{3+}$ and $Gd_2O_2S:Tb^{3+}$ is the width of the manifolds. The stronger crystal field in the oxide causes a larger splitting of the lines than that in the oxysulfide. All the transition clusters from the Tb^{3+} ion presented in Fig. 7b and d manifest the characteristic that the oxide transition manifolds are substantially wider than the corresponding oxysulfide manifolds.

The PL spectra presented in Fig. 7b and d indicate that the $^5D_3 \rightarrow {}^7F_J$ (J = 3, 4, 5 and 6) transitions for the 2%Tb^{3+} series have virtually disappeared. This can be seen in more detail in Fig. 13.

The difference between the spectra of the 0.1%Tb^{3+} and 2% Tb^{3+} series shown in Fig. 13 was also found in the $(Y_{1-x}Gd_x)_2O_2S:Tb^{3+}$ phosphors; however, the difference was smaller for the Y-based materials because of applying a slightly different excitation wavelength.[10] The low spectral radiances of the $^5D_3 \rightarrow {}^7F_J$ transitions at 2 mol% Tb^{3+} in Fig. 13b are due to the cross relaxation between adjacent Tb^{3+} ions.[2,4] This energy flow is illustrated by the following equation:

$$Tb^{3+}(^5D_3) + Tb^{3+}(^7F_6) \rightarrow Tb^{3+}(^5D_4) + Tb^{3+}(^7F_0). \qquad (1)$$

Because of this cross relaxation, the emission arising from the $^5D_3$ state diminishes and the green emission of the $^5D_4 \rightarrow {}^7F_5$ transition increases. It can be seen in Fig. 13 that the $^5D_3 \rightarrow {}^7F_J$ transitions for the 2%Tb^{3+} series emit almost two orders of magnitude (at low x) less light than the corresponding transitions of the 0.1%Tb^{3+} series. The blue emission from the $^5D_3$ states of $(Lu_{1-x}Gd_x)_2O_2S$:0.1%Tb^{3+} is also weaker than the corresponding emission in $(Y_{1-x}Gd_x)_2O_2S$:0.1% Tb^{3+}.[10]

In Fig. 13a and b the maximum spectral radiance of the $^5D_3 \rightarrow {}^7F_5$ transition has been represented by H_{417}. This

Open Access Article. Published on 19 May 2017. Downloaded on 12/5/2025 9:16:28 AM.
This article is licensed under a Creative Commons Attribution 3.0 Unported Licence.

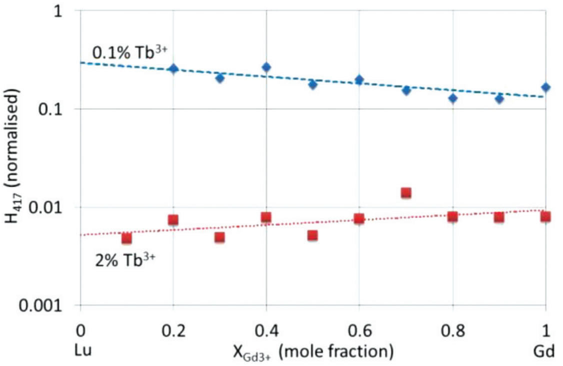

Fig. 14 Maximum normalised peak height of the $^5D_3 \rightarrow {}^7F_5$ transition (H_{417}) *versus* the composition parameter x of $(Lu_{1-x}Gd_x)_2O_2S:Tb^{3+}$. The excitation wavelength was 292 nm.

quantity is a good measure to quantify the colour changes of the PL of $(Lu_{1-x}Gd_x)_2O_2S$:0.1%Tb^{3+}, as we have shown previously. In Fig. 14 we have plotted H_{417} *versus* the mole fraction of Gd^{3+} in $(Lu_{1-x}Gd_x)_2O_2S:Tb^{3+}$. The data for the 0.1%$Tb^{3+}$ series indicate that H_{417} (and the other $^5D_3 \rightarrow {}^7F_J$ transitions) decreases upon increasing x_{Gd}, whereas the 2%Tb^{3+} series shows the opposite behaviour.

Because of the very low emission of the $^5D_3 \rightarrow {}^7F_5$ transition for the 2%Tb^{3+} series, it may be inferred that H_{417} does not change, confirming the fact that the there is no colour change for this phosphor series upon changing the ratio Lu/Gd.

For the 0.1%Tb^{3+} series the increase of H_{417} generates a colour change from cyan at $x_{Gd} = 0.1$ to green at $x_{Gd} = 1$. In this case, the cross relaxation presented in eqn (1) is insignificant, because of the larger average distance between neighbouring Tb^{3+} ions. Hence, in this phosphor series a second energy transfer process, which is dependent on the Lu/Gd ratio, becomes dominant. This will be explained hereafter.

In comparing the data represented in Fig. 14 to those in Fig. 11 of ref. 10 it is found that at $x_{Gd} = 1$ H_{417} for 2%Tb^{3+} is smaller than that in the previous work. The reason for this difference is the application of a different excitation wavelength, 292 nm in the present case and 270 nm in our work on $(Y_{1-x}Gd_x)_2O_2S:Tb^{3+}$. In Fig. 15 we have visualised the relevant energy flows upon exciting $(Lu_{1-x}Gd_x)_2O_2S$:0.1%Tb^{3+} and $(Y_{1-x}Gd_x)_2O_2S$:0.1%Tb^{3+} with UV light.

The energy flow represented in diagram 15a by the two arrows has been explained in detail in our previous work on $(Y_{1-x}Gd_x)_2O_2S:Tb^{3+}$.[10] The crucial point in this diagram is the location of the energy minima of the CT-bands of $Y_2O_2S:Tb^{3+}$ and $Gd_2O_2S:Tb^{3+}$: the level of $Y_2O_2S:Tb^{3+}$ is about 1000 cm^{-1} higher than that of $Gd_2O_2S:Tb^{3+}$. This allows energy to be transferred from the $^5D_3$ level in the latter compound, whereas this is impossible in $Y_2O_2S:Tb^{3+}$ at room temperature. For the solid solutions of $Y_2O_2S:Tb^{3+}$ and $Gd_2O_2S:Tb^{3+}$ we see a gradual transition when x_{Gd} is increased from 0 to 1 from no energy transfer to energy transfer. Diagram 15b represents the situation in the Lu–Gd system. The main difference with diagram 15a is the location of the CT-band of $(Lu_{0.8}Gd_{0.2})\ _2O_2S:Tb^{3+}$, which is very close to that of $Gd_2O_2S:Tb^{3+}$. This can be concluded from the red shift of the CT-bands represented in Fig. 11. The minimum of the CT band of $(Lu_{0.8}Gd_{0.2})_2O_2S:Tb^{3+}$ is expected to be slightly lower than the $^5D_3$ level, allowing a flow of energy from the latter to the CT-band, indicated by the second arrow. This explains the rather low value of H_{417} in Fig. 13 and the shallow slope of the 0.1%Tb^{3+} line in Fig. 14.

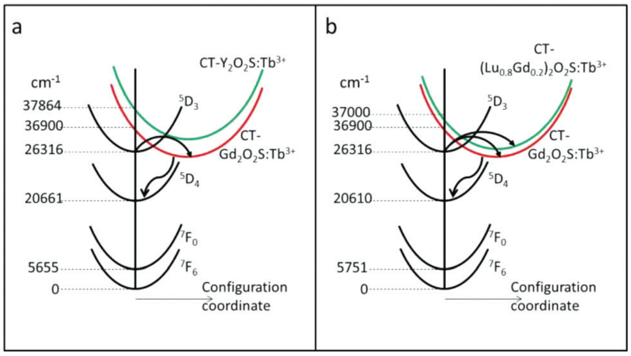

Fig. 15 (a): Configuration diagrams of $Gd_2O_2S:Tb^{3+}$ and $Y_2O_2S:Tb^{3+}$ and (b): configuration diagrams of $Gd_2O_2S:Tb^{3+}$ and $(Lu_{0.8}Gd_{0.2})\ _2O_2S:Tb^{3+}$. The configuration coordinates for the ^7F_J and ^5D_J levels are assumed to be equal for reasons of clarity.

Since the 100% Lu-samples consisted solely of 100% $Lu_2O_3:Tb^{3+}$, we profited from the opportunity to study the PL-spectra of these phosphors in more detail. Pure and Tb^{3+} doped Lu_2O_3 crystals have the cubic structure of the mineral bixbyite with 16 Lu_2O_3 molecules in one cell.[19] In Lu_2O_3 there are two different Lu^{3+} lattice sites, which possess the point symmetries C_2 and C_{3i}: 24 lattice sites have C_2 symmetry, while the other 8 have C_{3i} symmetry. Both sites are six coordinate and are thus present in the ratio of 3 : 1. Upon doping Lu_2O_3 with Tb^{3+} these lattice sites are occupied with Tb^{3+} with almost equal probability. Fig. 16 shows the excitation (a) and emission spectra (b) of Lu_2O_3:0.1%Tb^{3+}, in which the intensities are represented at linear scales in arbitrary units.

Details of the PL-spectra of Lu_2O_3:0.1%Tb^{3+} and Lu_2O_3:2% Tb^{3+} are partially presented in Fig. 17. For reasons of comparison the corresponding spectra of Y_2O_3:0.1%Tb^{3+} and Y_2O_3:3% Tb^{3+}, described in ref. 19, are represented in Fig. 18.

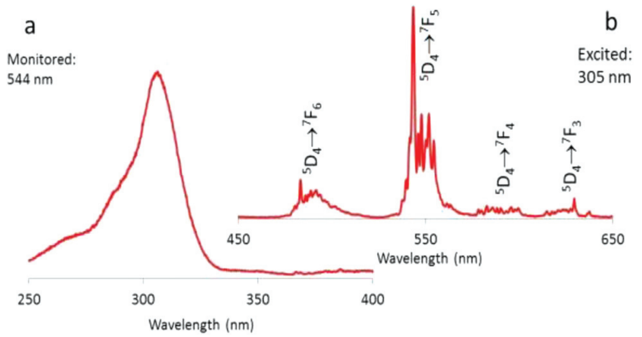

Fig. 16 Excitation (a) and emission spectra (b) of Lu_2O_3:0.1%Tb^{3+}. Vertical scales are linear and represent intensity in arbitrary units. The $^5D_3 \rightarrow {}^7F_J$ transitions at $\lambda < 475$ nm are too weak to be detected.

Open Access Article. Published on 19 May 2017. Downloaded on 12/5/2025 9:16:28 AM.
This article is licensed under a Creative Commons Attribution 3.0 Unported Licence.

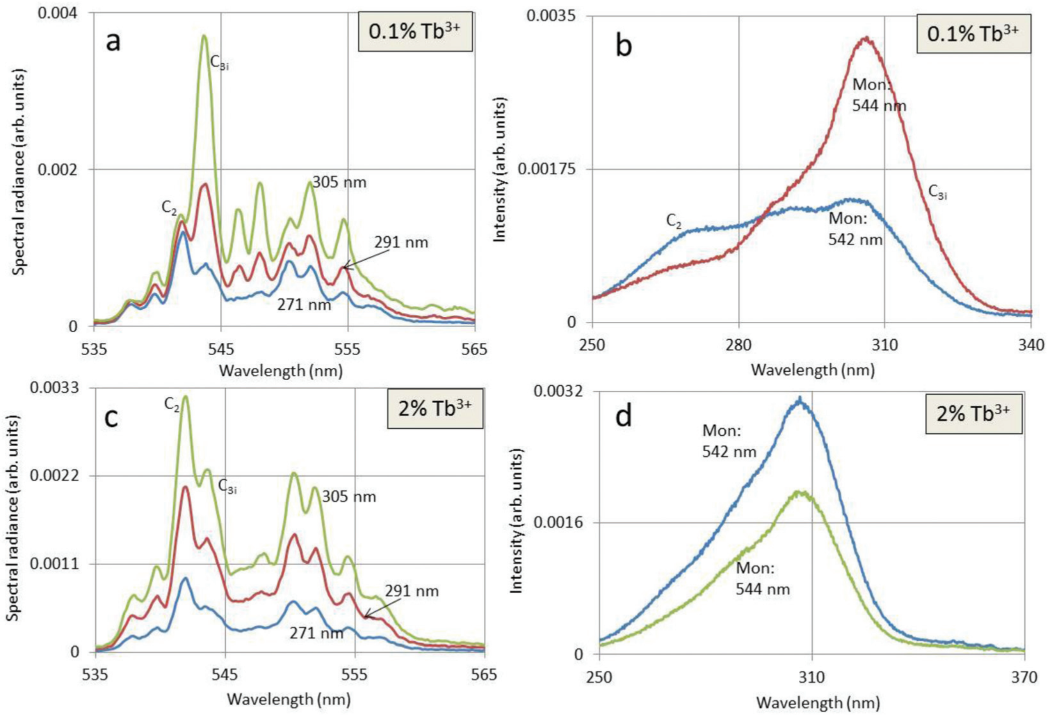

Fig. 17 (a): $^5D_4 \rightarrow {}^7F_5$ transition of Lu_2O_3:0.1%Tb^{3+} excited at three different wavelengths; (b) excitation spectra of Lu_2O_3:0.1%Tb^{3+} monitored at 542 nm and 544 nm; (c) $^5D_4 \rightarrow {}^7F_5$ transition of Lu_2O_3:2%Tb^{3+} excited at three different wavelengths; (d) excitation spectra of Lu_2O_3:2%Tb^{3+} monitored at 542 nm and 544 nm.

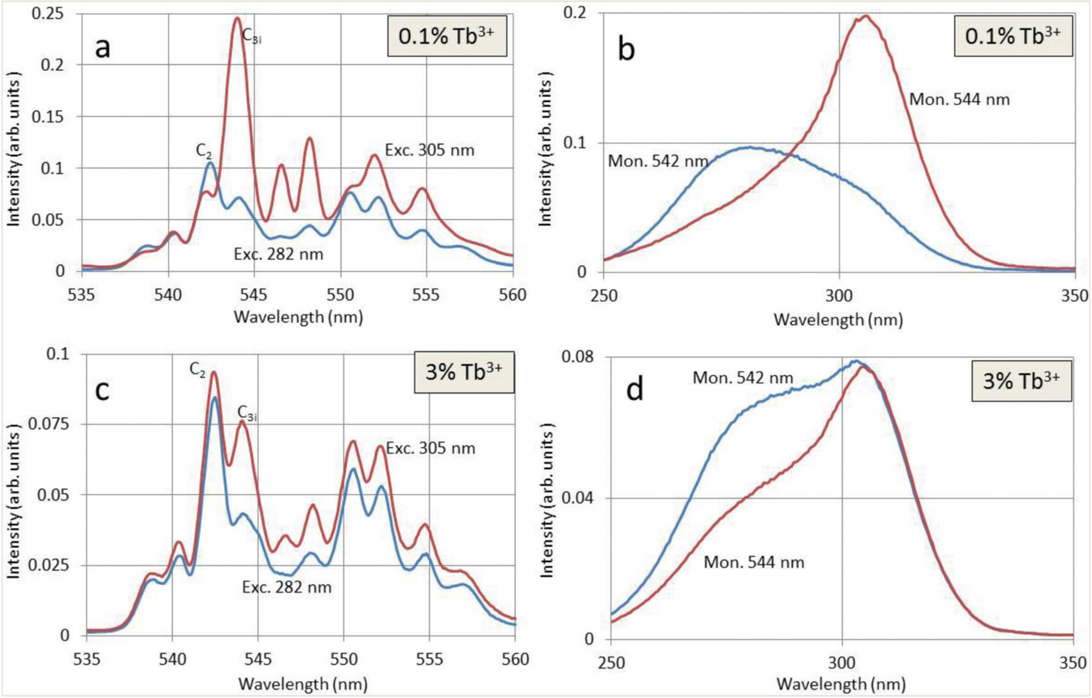

Fig. 18 (a) $^5D_4 \rightarrow {}^7F_5$ transition of Y_2O_3:0.1%Tb^{3+} excited at two different wavelengths; (b) excitation spectra of Y_2O_3:0.1%Tb^{3+} monitored at 542 nm and 544 nm; (c) $^5D_4 \rightarrow {}^7F_5$ transition of Y_2O_3:3%Tb^{3+} excited at two different wavelengths; (d) excitation spectra of Y_2O_3:3%Tb^{3+} monitored at 542 nm and 544 nm.[19]

This journal is © The Royal Society of Chemistry 2017

Open Access Article. Published on 19 May 2017. Downloaded on 12/5/2025 9:16:28 AM.
This article is licensed under a Creative Commons Attribution 3.0 Unported Licence.

In Fig. 17a the ratio of the peaks at 542 and 544 nm is seen to depend strongly on the excitation wavelength. This behaviour was also found in ref. 19; hence, due to the similar behaviour found in Y_2O_3:0.1%Tb^{3+}, shown in Fig. 18a, the 542 nm peak is attributed to Tb^{3+} in a C_2 site and the 544 nm peak refers to Tb^{3+} in a C_{3i} site. The excitation spectra of Lu_2O_3:0.1%Tb^{3+} represented in Fig. 17b differ slightly from these of Y_2O_3:0.1%Tb^{3+} in Fig. 18a, because the first shows an additional maximum at 271 nm. The differences between the PL spectra of Lu_2O_3:2%Tb^{3+} (Fig. 18c and d) and Y_2O_3:3%Tb^{3+} (Fig. 18c and d) are substantial. Fig. 17c does not show much difference between the ratios of the C_2 and C_{3i} peaks, whereas this ratio changes clearly in Fig. 18c. Furthermore, the C_2-type excitation spectrum monitored at 542 nm in Fig. 17d does not convincingly exhibit the hump at 280 nm, which is clearly present in the C_2-spectrum of Y_2O_3:3%Tb^{3+} (monitored at 542 nm) in Fig. 18d.

In the next paragraphs we shall consider why we could not synthesise pure $Lu_2O_2S:Tb^{3+}$. Although we have found from various repeats that the reproducibility of synthesising $(Lu_{1-x}Gd_x)_2O_2S:Tb^{3+}$ was poor from a yield point of view, some conclusions on what was going on can be made. The first conclusion is that at $x = 0$ (100% Lu) we could not make any oxysulfide. The second is that at $x > 0.7$ (high Gd concentration) we made 100% oxysulfide in one phase. For the intermediate Gd concentrations we obtained incomplete sulfurization. The third conclusion is that the deviation of the cell constants from Vegard's law for the oxide oxysulfide phases can be interpreted in terms of segregation: the oxide phase is enriched with Lu and the oxysulfide phases (notably OS-2) are enriched with Gd. Finally, the presence of two oxysulfide phases in the samples with $0.1 < x < 0.7$ is beyond doubt. In the subsequent discussion we shall first consider what can be concluded from thermodynamics.

Unlike the lanthanide sesquioxides,[23,24] rare earth oxysulfides do not have a complete record of thermodynamic data.[25,26] The formation enthalpy of Gd_2O_2S has been reported by Andreev *et al.* recently.[25] From that information and a calculation of the lattice energy and Born–Haber analysis, we have calculated the formation enthalpy of Lu_2O_2S. The lattice energy U_{Ln} of Ln_2O_2S, where Ln is Gd, Y or Lu, can be calculated with the Madelung equation that contains the repulsion term $1/b$:

$$U_{\mathrm{Ln}} = -1.44\frac{M}{d_{\mathrm{Ln-O}}}\left(1-\frac{1}{b}\right), \tag{2}$$

where M is the Madelung constant for the molecule Ln_2O_2S in the hexagonal $P\bar{3}m1$ lattice and $d_{\mathrm{Ln-O}}$ is the shortest distance between the lanthanide ion and the oxygen anions. When $d_{\mathrm{Ln-O}}$ is expressed in nm, U_{Ln} is expressed in eV. The Madelung constant for hexagonal Ln_2O_2S is 24.179.[27] The dimensionless repulsion parameter b is usually between 6 and 9 for inorganic crystals.[24] The values for $d_{\mathrm{Ln-O}}$ for the Gd, Y and Lu oxysulfide are 0.226 nm, 0.223 nm and 0.2219 nm (ref. 10) respectively, where the latter value has been estimated from the ratios between the cell dimensions of Y_2O_2S and Lu_2O_2S. The result of this analysis is represented in Table 4.

Table 4 Lattice energy and standard formation enthalpy of Ln_2O_2S in kJ mol^{-1}

	Gd	Y	Lu
U_{Ln}	−12 329	−12 513	−12 558
ΔH	−1650[a]	−1766	−1546

[a] Taken from ref. 25.

The repulsion parameter b was assumed to be identical for Gd_2O_2S, Y_2O_2S and Lu_2O_2S and calculated to be 5.87 from the known value of ΔH for Gd_2O_2S. Although the repulsion parameter seems to be rather low, the result for Lu_2O_2S is in line with the Born–Haber analysis of Ln_2O_3 made by Morss.[24] In accepting this result, it can be concluded that the difference between the standard formation enthalpies of Lu_2O_2S and Gd_2O_2S is so small that it cannot explain the observed phenomena represented in Fig. 3. If b would be larger for Lu_2O_2S, the standard enthalpy of formation becomes more negative, indicating higher stability. In other words, this quasi thermodynamic analysis does not explain why we could not synthesise $Lu_2O_2S:Tb^{3+}$.

We shall propose therefore a kinetic argument that explains the high oxide content at low x in $(Lu_{1-x}Gd_x)_2O_2S:Tb^{3+}$ as shown in Fig. 3. Let's assume that the hydroxy carbonate precursor first decomposes into $(Lu_{1-x}Gd_x)_2O_3:Tb^{3+}$ during the annealing step at 900 °C. The fact that Lu_2O_2S is known to only form under high sulfur pressure indicates that Lu_2O_3 does not accommodate S^{2-} anions readily and does not easily convert from Lu_2O_3 to Lu_2O_2S. Following on from this reasoning and the unit cell constants of Ln_2O_3 published by Morss,[24] it appears that for $(Lu_{0.9}Gd_{0.1})O_3$ only a relatively small amount of the oxysulfide structures form. This would mean that $(Lu_{0.9}Gd_{0.1})O_3$ is tight and does not easily open to allow more S^{2-} anions to diffuse into its structure. For the compounds $(Lu_{1-x}Gd_x)O_3$, in which $x = 0.2$ or more, progressively larger amounts of the oxy-sulfide lattice form till an x value of around 0.7 when no oxide phase remains. Thus the $(Lu_{1-x}Gd_x)O_3$ cell needs to increases in size substantially before enough S^{2-} anions can diffuse in to completely convert all the oxide to oxy-sulfide.

The question that still needs to be addressed is the formation of the two oxysulfide phases shown in Fig. 3. In addition to what has been mentioned in the previous paragraph, we also could assume that there are two routes to form the oxysulfide instead of only one: route 1 is the direct sulfurization of hydroxy carbonate, which is assumed not to lead to segregation and yielding mainly OS-1. In route 2 it is assumed that the hydroxy carbonate is largely decomposed and forms the cubic oxide. For small x (high Lu content) it is difficult for the bulky sulfur atom to enter the crystal; only after segregation, in which a part of the oxide gets more Gd

Open Access Article. Published on 19 May 2017. Downloaded on 12/5/2025 9:16:28 AM.
This article is licensed under a Creative Commons Attribution 3.0 Unported Licence.

(and another part is enriched with Lu), the Gd-rich part can be converted into the oxysulfide, while the part that is Lu-rich cannot be converted. For large x the oxide lattice is supposed to be sufficiently swollen to allow the sulfur atoms to penetrate, diffuse and complete the sulfurization. The separate experiment of the sulfurization of $(Lu_{0.4}Gd_{0.6})_2O_3$:2% Tb^{3+} at 900 °C indicated that the cell constants of the oxide before sulfurization were 10.608 Å and 10.672 Å (average 10.640 Å), as shown in Table 3, whereas after sulfurization the cell constant of the small remaining oxide concentration had shrunk to 10.568 Å (Table 2, note 5). This result confirms that during sulfurization of the oxide segregation is taking place. From these considerations we infer that routes 1 and 2 occur simultaneously and that route is 2 is (slightly) prevailing.

Conclusions

From the work presented here it can be concluded that $(Lu_{1-x}Gd_x)_2O_2S:Tb^{3+}$ phosphors are efficient green emitting phosphors. These phosphors show only a modest colour change upon varying the Lu/Gd ratio for the 0.1%Tb^{3+} series, whereas virtually no colour change was observed for the 2% Tb^{3+} series. This is different for the $(Y_{1-x}Gd_x)_2O_2S:Tb^{3+}$ phosphors, which manifest a substantial colour change upon changing x. This difference could be explained in terms of a slight change of the energy transfer. In the case of $(Lu_{1-x}Gd_x)_2O_2S:Tb^{3+}$ the energy transfer from the $^5D_3$-level of Tb^{3+} to the minimum of the CT-band starts already at 10% Gd (high Lu content). This could be inferred from a smaller red shift of the CT-band of $(Lu_{1-x}Gd_x)_2O_2S:Tb^{3+}$ than that of $(Y_{1-x}Gd_x)_2O_2S:Tb^{3+}$. We also found that $Lu_2O_2S:Tb^{3+}$ and $Gd_2O_2S:Tb^{3+}$ do not form a solid solution when synthesized in the way as we have described; this also deviates from the behaviour observed in the Y–Gd oxysulfide system. The synthesis of $(Lu_{1-x}Gd_x)_2O_2S:Tb^{3+}$ by annealing the hydroxy carbonate precursor in a CO_2/S atmosphere did not yield pure oxysulfide samples at $x < 0.7$. This apparent drawback turned out to be in fact a rather unique opportunity to study the oxide phase in addition to the oxysulfide. At $x = 0$ (no Gd) we obtained 100% $Lu_2O_3:Tb^{3+}$, which enabled the study of the symmetry-related properties of the $^5D_4 \rightarrow {}^7F_5$ Tb^{3+} transition of $Y_2O_3:Tb^{3+}$. The presence of oxide in the samples also enabled an estimate of the difference of the quantum efficiency between $Gd_2O_2S:Tb^{3+}$ and $Lu_2O_3:Tb^{3+}$; *viz*. $(Lu_{1-x}Gd_x)_2O_2S:Tb^{3+}$ (at $x > 0.5$), which is more than one order of magnitude more efficient than $Lu_2O_3:Tb^{3+}$. This finding makes the $(Lu_{1-x}Gd_x)_2O_2S:Tb^{3+}$ phosphors with $0.2 < x < 0.6$ an attractive option for X-ray intensifying screens because of their high efficiency and density.

Acknowledgements

We are grateful to the EPSRC and Technology Strategy Board (TSB) for funding the PURPOSE (TP11/MFE/6/1/AA129F; EP-SRC TS/G000271/1) and CONVERTED (JeS no. TS/1003053/1), PRISM (EP/N508974/1) and FAB3D programs. We are finally grateful to the TSB for funding the CONVERT program.

References

1 L. Ozawa, *Cathodoluminescence- Theory and Applications*, Kodansha/VCH, Tokyo, Japan/Weinheim, Germany, 1990.
2 X. Yan, G. R. Fern, R. Withnall and J. Silver, *Nanoscale*, 2013, **5**, 8640.
3 X. Yan, G. R. Fern, R. Withnall and J. Silver, *Nanoscale*, 2013, **5**, 1091.
4 J. Silver, X. Yan, G. Fern and N. Wilkinson, Proceedings of the 20th International Display Workshops, IDW'13, 2013, p. 823.
5 G. R. Fern, X. Yan, N. Wilkinson and J. Silver, Proceedings of the 20th International Display Workshops, IDW'13, 2013, p. 820.
6 R. Withnall, J. Silver, T. G. Ireland, A. Lipman, G. R. Fern and P. Saxty, SID International Symposium Digest of Technical Papers, 2005, vol. 36, p. 594.
7 N. Miura, in *Phosphor Handbook*, ed. S. Shionoya, W. M. Yen and H. Yamamoto, CRC Press, Boca Rotan, Florida, 2nd edn, 2006, ch. 7.
8 G. Blasse and B. C. Grabmaier, *Luminescent Materials*, Springer-Verlag, Berlin, 1994.
9 C. W. E. van Eijk, *Phys. Med. Biol.*, 2002, **47**, R85.
10 R. Brüninghoff, D. den Engelsen, G. R. Fern, T. G. Ireland, R. Dhillon and J. Silver, *RSC Adv.*, 2016, **6**, 42561.
11 J. Zhao, C. Guo, L. Zhang and J. Hu, *J. Lumin.*, 2007, **122–123**, 924.
12 G. Wang, H. Zou, H. Zhang, L. Gong, Z. Shi, X. Xu and Y. Sheng, *Mater. Lett.*, 2014, **128**, 256.
13 B. Zhang, H. Zou, Y. Dai, Y. Song, K. Zheng, X. Zhou and Y. Sheng, *RSC Adv.*, 2016, **6**, 7846.
14 R. D. Shannon, *Acta Crystallogr., Sect. A: Cryst. Phys., Diffr., Theor. Gen. Cryst.*, 1976, **32**, 751.
15 J. Silver, T. Ireland and G. Fern, 231st ECS Meeting, 2015, http://ma.ecsdl.org/content/MA2015-02/38/1575.abstract.
16 D. den Engelsen, G. R. Fern, P. G. Harris, T. G. Ireland and J. Silver, *Materials*, 2017, **10**, 312.
17 A. A. da Silva, M. A. Cebim and M. R. Davolos, *J. Lumin.*, 2008, **128**, 1165.
18 E. I. Gorokhova, V. A. Demidenko, O. A. Khristich, S. B. Mikhrin and P. A. Rodnyǐ, *J. Opt. Technol.*, 2003, **70**, 693.
19 D. den Engelsen, P. G. Harris, T. G. Ireland, G. Fern and J. Silver, *ECS J. Solid State Sci. Technol.*, 2015, **4**, R145.
20 B. Zhang, H. Zou, H. Guan, Y. Dai, Y. Song, X. Zhou and Y. Sheng, *CrystEngComm*, 2016, **18**, 7620.
21 P. Yang, S. Gai, Y. Liu, W. Wang, C. Li and J. Lin, *Inorg. Chem.*, 2011, **50**, 2182.
22 A. Lempicki, C. Brecher, P. Szupryczynski, H. Lingertat, V. V. Nagarkar, S. V. Tipnis and S. R. Miller, *Nucl. Instrum. Methods Phys. Res., Sect. A*, 2002, **488**, 579.

This journal is © The Royal Society of Chemistry 2017

Open Access Article. Published on 19 May 2017. Downloaded on 12/5/2025 9:16:28 AM.
This article is licensed under a Creative Commons Attribution 3.0 Unported Licence.

23 R. J. M. Konings, O. Beneš, A. Kovács, D. Manara, D. Sedmidubský, L. Gorokhov, V. S. Iorish, V. Yungman, E. Shenyavskaya and E. Osina, *J. Phys. Chem. Ref. Data*, 2014, **43**, 013101.

24 L. R. Morss, *Chem. Rev.*, 1976, **76**, 827.

25 P. O. Andreev, E. I. Sal'nikova and I. M. Kovenski, *Inorg. Mater.*, 2014, **50**, 1018.

26 J. W. Haynes and J. J. Brown, *J. Electrochem. Soc.*, 1969, **115**, 1061.

27 Q. C. Johnson and D. H. Templeton, *J. Chem. Phys.*, 1961, **34**, 2004.